Article

Yttria-Coated Tungsten Fibers for Use in Tungsten Fiber-Reinforced Composites: A Comparative Study on PVD vs. CVD Routes

Saravanan Palaniyappan [1,*] , **Maik Trautmann** [1] , **Yiran Mao** [2] , **Johann Riesch** [3] , **Parikshith Gowda** [1] , **Nick Rudolph** [1] , **Jan Willem Coenen** [2] , **Rudolf Neu** [3,4] **and Guntram Wagner** [1]

[1] Group of Composites and Material Compounds, Institute of Materials Science and Engineering (IWW), Chemnitz University of Technology, 09125 Chemnitz, Germany; maik.trautmann@mb.tu-chemnitz.de (M.T.); parikshith-gowda.kabbare-ramalingaiah@mb.tu-chemnitz.de (P.G.); nick.rudolph@mb.tu-chemnitz.de (N.R.); guntram.wagner@mb.tu-chemnitz.de (G.W.)

[2] Forschungszentrum Jülich GmbH, Institut für Energie- und Klimaforschung Plasmaphysik, Partner in the Trilateral Euregio Cluster, 52425 Jülich, Germany; y.mao@fz-juelich.de (Y.M.); j.w.coenen@fz-juelich.de (J.W.C.)

[3] Max Planck Institute for Plasma Physics (IPP), 85748 Garching, Germany; johann.riesch@ipp.mpg.de (J.R.); rudolf.neu@tum.de (R.N.)

[4] Group of Plasma Component Interaction, Technical University Munich, 85748 Garching, Germany

* Correspondence: saravanan.palaniyappan@mb.tu-chemnitz.de; Tel.: +49-371-531-33873

Abstract: Tungsten fiber-reinforced tungsten (W_f/W) composites are being developed to improve the intrinsic brittleness of tungsten. In these composites, engineered fiber/matrix interfaces are crucial in order to realize toughening mechanisms. For such a purpose, yttria (Y_2O_3), being one of the suitable interface materials, could be realized through different coating techniques. In this study, the deposition of thin films of yttria on a 150 μm tungsten wire by physical and chemical vapor deposition (PVD and CVD) techniques is comparatively investigated. Although fabrication of yttria is feasible through both CVD and PVD routes, certain coating conditions such as temperature, growth rate, oxidation of W_f, etc., decide the qualitative nature of a coating to a particular extent. In the case of PVD, the oxidation of W_f is highly reduced compared to the WO_3 formation in high-temperature CVD coating processes. Yttria-coated tungsten fibers are examined comprehensively to characterize their microstructure, phase, and chemical composition using SEM, XRD, and Raman spectroscopy techniques, respectively.

1. Introduction

Fusion energy is an attractive option when searching for potential sources of energy, due to its virtually inexhaustible supply of fuel and its guarantee of minimal adverse environmental impacts [1]. While major research and development studies for fusion reactor technology have been performed, there is still a long way to go for fusion to enter the market for commercial energy. In addition to issues related to plasma physics, one of the unanswered concerns is the power and particle exhaust of a fusion reactor, and thus the material issues related to the plasma-facing materials (PFM) [2,3]. In terms of the armor material of a divertor—the component with the highest heat and particle load—these significant challenges require advanced measures in areas spanning from mechanical strength to thermal properties [4]. High heat loads and large numbers of neutrons cause recrystallization, melting, and displacement damage, which impact the actual microstructure of the material [5]. Plasma ions impacting the surface cause surface morphology changes and erosion by sputtering [6]. Tungsten is a suitable PFM since it is resilient against sputtering, has the highest melting point of any metal, and shows rather

benign behavior under neutron irradiation [7]. Nonetheless, tungsten also faces several problems that have yet to be resolved: room temperature brittleness, overall low fracture resistance, neutron irradiation embrittlement, and recrystallization [8,9].

To resolve the intrinsic brittleness of tungsten, tungsten fiber-reinforced tungsten (W_f/W) composites are being intensively developed using the well-known concept of fiber-reinforced ceramic matrix composites (FCMCs) [10–12]. Commercial tungsten wires with high strength and decent ductility (fracture strain > 2% @ r.t.) are used to reinforce the brittle tungsten matrix. When a matrix crack meets an array of fibers perpendicular to the crack plane, the crack can deflect along the interfaces. The fibers hinder the primary opening crack and suppress its dynamic propagation [13–15]. Here, a relatively "weak" interphase is the key factor to achieve the desired pseudo-ductility and allows for energy dissipation mechanisms during cracking [10,16,17]. "Weak" interface debonding before fiber failure is the precondition of multiple energy dissipation mechanisms, such as crack deflection, fiber bridging, and fiber pull-out. Oxides are one option regarding interface materials, as they are brittle in nature and contain micro-cracks. Therefore, they are porous enough to incorporate the behavior of crack deflection and allow mechanisms of pseudo-ductility to occur [18].

Yttrium oxide or yttria (Y_2O_3) is chemically and structurally very similar to other oxides of the rare earth elements, and thus falls into the rare earth sesquioxide group. It is a ceramic material that is of great industrial and technological utility [19–21]. Yttria is an ideal candidate for the interface material for W_f/W composites due to its good thermal and chemical stability [22,23]. Additionally, it shows low activation after neutron irradiation, which is particularly important for a fusion reactor [24].

For realizing interfacial yttria coatings on W_f, there are several thin-film coating technologies available, such as atomic layer deposition, reactive magnetron sputtering, etc. [25,26]. Among these, the coating process that is widely used for producing yttrium oxide coating on tungsten fibers (i.e., magnetron sputtering) is not very efficient in terms of production. The production rate of interface coating is relatively low; it is time consuming and extensive material consuming, making it a bottleneck in the preparation of the W_f/W composites [12]. To resolve this issue, an alternative coating process is desirable, as it offers both high production rates and optimal coating quality.

Chemical vapor deposition (CVD) is potentially one of the coating processes that might create a more economic coating on W fibers, due to its fast deposition rate and mass production with a considerably reduced amount of material usage. In this study, both CVD and PVD process routes are used to prepare the yttrium oxide coating of tungsten fibers. The microstructure, crystalline phase compositions, and chemical compositions of the coatings were analyzed using SEM, XRD, and Raman spectroscopy, respectively. A comparative summary of the analyses is provided in the results and discussions section.

2. Materials and Methods

2.1. Fabrication Techniques

2.1.1. Chemical Vapor Deposition

For the fabrication of Y_2O_3 on single filament tungsten fibers (W_f) with 150 μm in diameter and 260 mm in length (K wire Type B; OSRAM GmbH, Schwabmünchen, Germany), a metal–organic chemical vapor deposition (MOCVD) technique was employed. The tungsten fibers were pre-treated using acetone/5 wt.% NH_4OH at 80 °C for 30 min to remove the natural oxide layer from the surface of W_f. The metal–organic precursor tris (2,2,6,6-tetramethyl-3,5-heptane-dionato)yttrium; 98% (99.9%-Y) (Y (TMHD)$_3$) from abcr GmbH (Karlsruhe, Germany), was chosen because of its stability and low volatizing temperature (175 °C) [27]. The experiments were conducted in an MOCVD chamber (FHR Anlagenbau GmbH, Ottendorf-Okrilla, Germany) that was composed of a horizontal glass reactor in which three heaters (H1, H2, and H3) were equipped, as shown in Figure 1. The metal–organic precursor was placed in a ceramic crucible at one end of the chamber with a thermocouple (TC) to simultaneously read the volatizing temperature of the precursor. The carrier gas Argon (Ar, 99.9999% purity), forming gas (H_2, 99.9999% purity), and reaction

gas (O_2, 99.9999% purity), all from Air Liquide Deutschland GmbH—Düsseldorf, Germany, were released into the chamber once the desired coating temperature was reached in heater H2 and the volatizing temperature was approached, based on the TC. Three different temperatures were maintained at different regions of the MOCVD chamber (H3 > H2 > H1), using three separate heaters (H1, H2, and H3), as shown in Figure 1. The lowest temperature was maintained at H1, so that the temperature around the TC did not exceed the volatizing temperature of the precursor. The temperature maintained at H2 was the actual deposition temperature of the yttria coating on tungsten fibers placed in the middle of the chamber. The higher temperature maintained at H3 assists in the evacuation of the carrier gas and undesired by-products without becoming condensed onto the walls of the MOCVD chamber. The amount of precursor, chamber pressure, and coating time are always kept constant to avoid any influence of these parameters on the thickness of the fabricated yttrium oxide coatings. Similarly, the temperature at all the three heaters (H1, H2, and H3) is maintained as constant during the coating time period of 150 min.
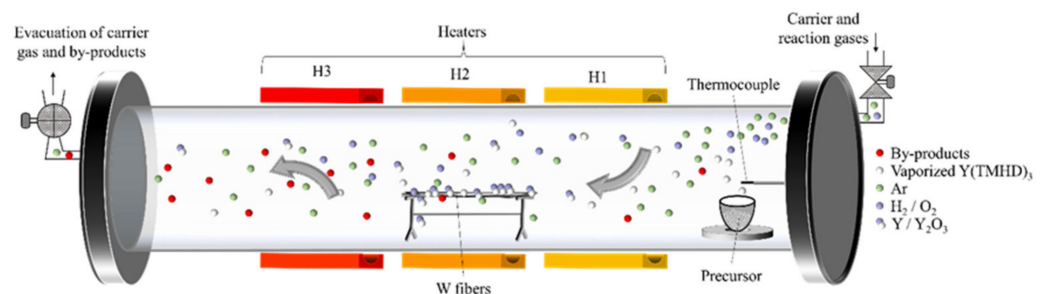

Figure 1. General schematic for the discontinuous MOCVD of Y/Y_2O_3 on W_f.

The following two strategies were used for the fabrication of Y_2O_3 with reduced oxidation of W_f during the high-temperature MOCVD coating process:

1. Indirect method of coating metallic yttrium on W_f in a hydrogen atmosphere (CVD_Y_H_2) followed by post-annealing (PA) in the same CVD chamber at 560 °C for 30 min in an O_2 atmosphere to form Y_2O_3 on the W_f (CVD_Y_H_2 + PA).
2. Direct method of coating yttrium oxide on W_f in an O_2 atmosphere (CVD_Yt_O_2) without any post-processing. The detailed coating parameters used for the two strategies are shown in Table 1.

Table 1. Experimental strategies with used parameters for the MOCVD process.

Strategies	Mass of Precursor Y (TMHD)$_3$	Pressure	Ar/H$_2$/O$_2$ Flow	Chamber Temperature H3/H2/H1	Post Annealing (PA)
-	g	mbar	sccm	°C	-
1.	0.70	1.5	66/33/0	650/525/320	560 °C/ 30 min/O$_2$
2.	0.70	1.5	75/0/25	650/550/320	-

2.1.2. Physical Vapor Deposition (RF-Magnetron Sputtering)

For comparison, yttrium oxide coating was also prepared by a reactive magnetron sputtering process using a Prevac magnetron sputtering system [28]. The magnetron target material was yttrium metal (Kurt J. Lesker Company, 99.9% purity, 76.2 mm diameter, 6.35 mm thickness). Argon was used for sputtering (~25 sccm). The distance between the target and the substrate was ~15 cm. Oxygen was injected as reactive gas (~2.5 sccm), so that yttrium oxide could be formed. The oxygen inlet position was around the same as the sample stage. An RF power supply with 13.45 MHz frequency was used to avoid the arcing effect of a DC power supply [29,30]. The transmitter power was 350 W. During the

deposition process, the sample stage was rotated with a speed of 20°/s to guarantee the homogeneous distribution of the deposition. The substrate temperature during deposition reached ~140 °C due to the kinetic energy and heat of condensation of coating atoms and plasma radiation. The vacuum chamber background pressure was ~5×10^{-8} mbar and the pressure during deposition was ~6.5×10^{-3} mbar. The short tungsten fibers were coated by a magnetron sputtering process, as described in [12]. In the first step, one layer of short fibers was spread on a flatbed, which was then put into the magnetron for the first deposition process. As a result, one side of the fibers was coated. In the second step, the short fibers were flipped with the help of another flatbed, and a second coating step was applied in sequence. By doing so, the whole circumferential surface of each of the short single fiber is coated almost homogeneously.

2.2. Characterization Techniques

2.2.1. Raman Spectroscopy

Raman spectroscopy characterizations of the yttria-coated W_f were carried out using an inVia™ Raman spectrometer (Renishaw GmbH, Pliezhausen, Germany). A Green laser (Nd: YAG) with a wavelength of 532 nm and a laser power of 50 mW was used to illuminate the coated fiber surface. The Raman spectra were collected by accumulating 25 single spectral measurements, with each accumulation lasting for 1 s. By using single laser spot measurements, the samples were analyzed on 5 different positions (along the axis of the coated fiber) for each of the parameter sets to check the repeatability of the detected chemical compositional phases.

2.2.2. X-ray Diffractometry

XRD phase analyses on the Y_2O_3-coated W_f were carried out using a diffractometer (Bruker, D8 Discover, Karlsruhe, Germany) with Co–Kα radiation. The XRD samples were analyzed by a point focus beam using a 0.5 mm pinhole aperture and a LynxEye XE–T detector (Bruker, Karlsruhe, Germany) for a measurement time of approximately 24 h.

2.2.3. Scanning Electron Microscopy

For the microstructural characterization of the yttria/yttrium coated W_f, a scanning electron microscope from Carl Zeiss (NEON 40EsB, Oberkochen, Germany) was used. The microstructure of the fracture surface of non-coated and coated fibers was analyzed. To obtain the fracture surface, the coated fibers were cut using a metal cutter that caused the delamination of the coating to a small extent, as seen in Figure 2. The standard cross-section preparation using metallographic techniques was not used in order to avoid the extensive delamination caused by the thermal expansion coefficient mismatch between the substrate (W_f), coating material (Y_2O_3), and the embedding polymer (Epoxy).
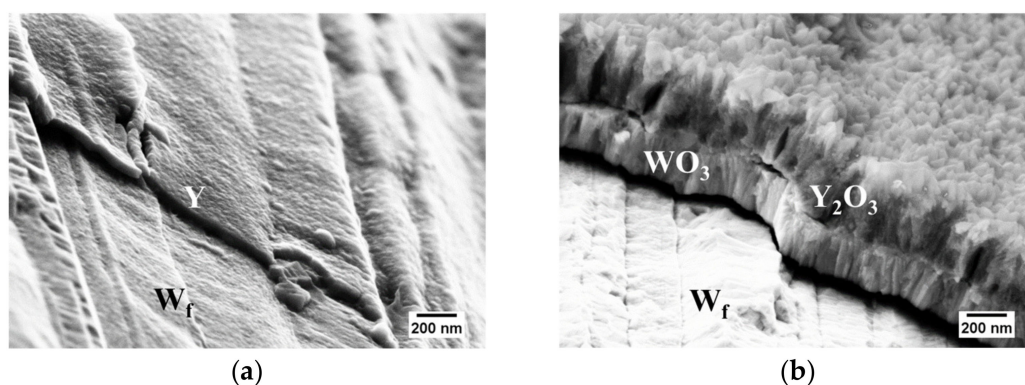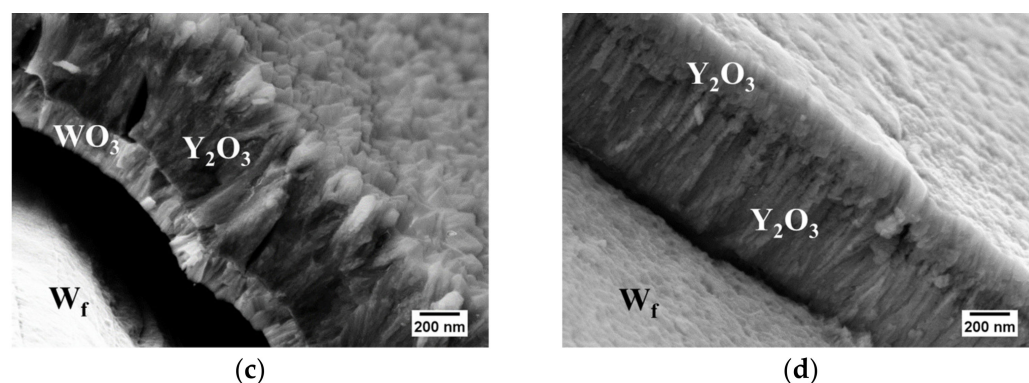

(**a**)   (**b**)

Figure 2. *Cont.*

(**c**) (**d**)

Figure 2. The SEM fracture surfaces of (**a**) CVD_Y_H$_2$, (**b**) CVD_Y_H$_2$ + PA, (**c**) CVD_Yt_O$_2$, and (**d**) PVD samples (delamination seen between the W$_f$ and the coating is caused by the cutting technique used to obtain the fracture surface).

3. Results and Discussions

3.1. Microstructural Analysis

Upon analyzing the microstructure of the CVD-coated fibers, it was observed that Y$_2$O$_3$ was homogeneously coated on the fibers in both of the two experimental strategies with varied gas flow parameters. The only differences are in the thickness and the way they bonded with the substrate. The WO$_3$ is also formed during both fabrication strategies, which is evidenced from the XRD results. Moreover, the multilayer-like CVD coating (two separate growth structures) the W fibers could be composed of WO$_3$/Y$_2$O$_3$. A layer of WO$_3$ is formed because of the high-temperature coating system used during the CVD process.

The fracture surfaces of the coated fibers are shown in Figure 2. The CVD_Yt_O$_2$ has a thicker coating of Y$_2$O$_3$ compared to the CVD_Y_H$_2$ + PA, although the coating time used is constant in both the strategies. This could be due to the post-annealing process (560 °C/30 min/O$_2$ atmosphere), which led to the formation of a thicker WO$_3$ beneath the Y$_2$O$_3$ coating. This shows that the CVD_Yt_O$_2$ parameters are optimal for reducing the oxidation of W fibers along with pre-treatment effects. The delamination effect seen on the fiber fracture surface is attributed to the used fiber cutting technique that delaminates the coating to a small extent.

In the PVD coatings, the formation of WO$_3$ is avoided, as the coating temperature is maintained below the oxidation temperature of W$_f$ (399 °C). While a homogeneous coating on the fiber is evidenced, the coating is not even throughout the axial length of the short fibers, and it also depends on the distance of the short fibers relative to the center of the sputter target. Therefore, the coating thickness shows a larger variation, depending on the positions of the short fibers in the magnetron device. The two-layer structure observed is due to the flipping of the fiber surface on a flatbed during the fabrication process. The surface morphology of the fabricated yttria coatings appear completely different when using different coating technologies like PVD and CVD techniques. The PVD-coated yttria has a less rough Yttria surface compared to a more rougher Yttria surface on the CVD-coated W$_f$. A columnar grain orientation is observed in PVD coating, whereas a random orientation of grains is observed in CVD yttria coatings. The thickness of the WO$_3$/Y$_2$O$_3$ coatings was measured using ImageJ software [31] at 15 different positions on various fracture surface images obtained through SEM. A comparative graphical representation of the amount of formation of WO$_3$ in response to the fabrication of Y$_2$O$_3$ on W$_f$ is plotted in Figure 3.
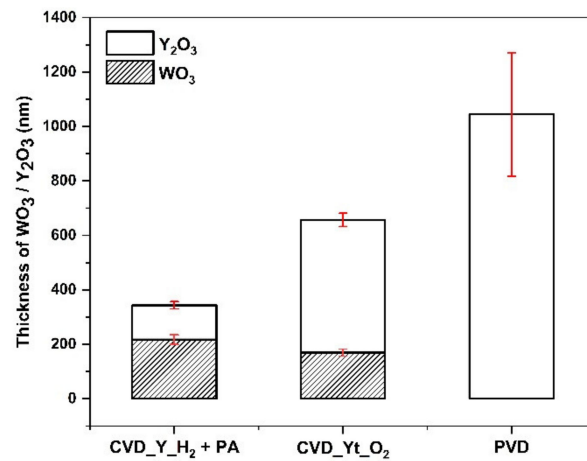
Figure 3. Graphical representation of the formation of WO$_3$ in response to the fabrication of Y$_2$O$_3$ on W$_f$ using CVD and PVD routes.

3.2. Raman Spectral Analysis

A comparative Raman spectroscopy analysis of the WO$_3$/Y$_2$O$_3$-coated W$_f$ through CVD and PVD is presented in Figure 4.
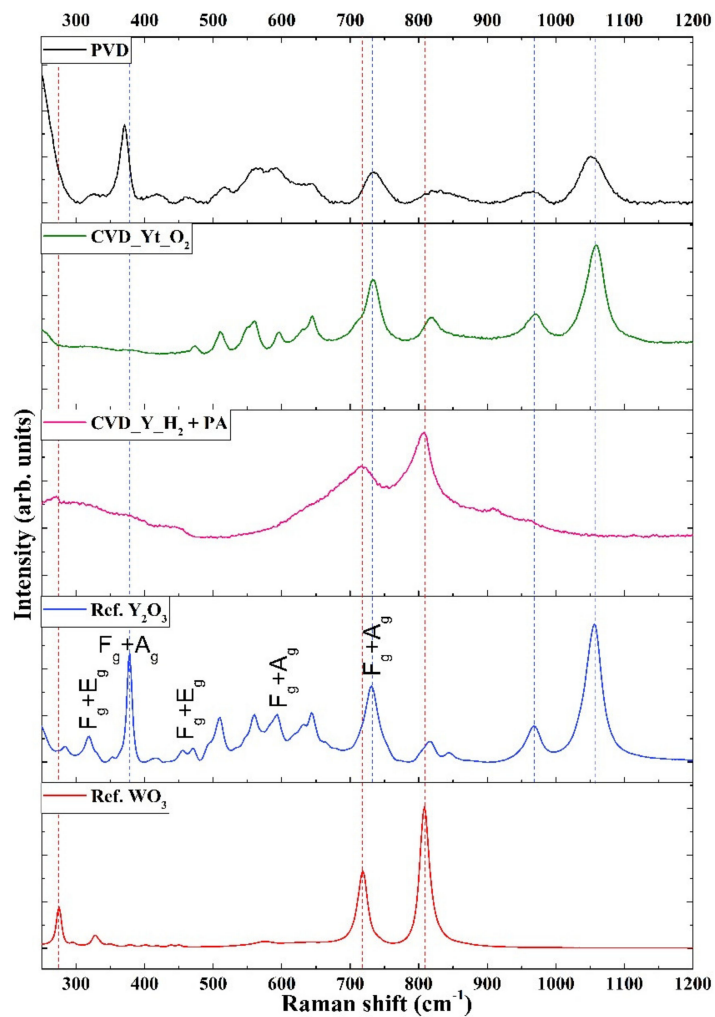

Figure 4. Raman spectra of CVD- and PVD-coated WO$_3$/Y$_2$O$_3$/W$_f$.

In the Raman spectra, the Y_2O_3 signal can only be detected in the PVD and CVD_Yt_O$_2$ samples. Even though a multilayer structure is identified through microstructural analysis of the CVD_Y_H$_2$ + PA samples, only signals of WO_3 are detected in this sample. It could be due to the fact that, in CVD_Y_H$_2$ + PA fibers, the Y_2O_3 layer is comparatively thinner than the penetration depth of the laser source used in Raman spectroscopy. This causes the illuminating laser source to penetrate through the thinner Y_2O_3 layer, and the molecular vibrations necessary for obtaining the Raman signal are happening at the intermediate thicker WO_3 layer, resulting in the provision of dominant WO_3 signals. This explanation is supported by the XRD analyses on the CVD_Y_H$_2$ + PA fibers, revealing a strong WO_3 diffraction peak in contrast to a weak Y_2O_3 diffraction peak, as shown in Figure 5. The peak at 377.77 cm^{-1} corresponds to the characteristic cubic structure of Y_2O_3 with an $F_g + A_g$ vibration mode [32], and it is predominantly evidenced in PVD-coated fibers. The peaks present at around 319.07, 470.67 and 592.26 cm^{-1} could be attributed to the $F_g + E_g$ as well as the $F_g + A_g$ vibration modes [32] of Y_2O_3, which is predominant in the CVD-coated fiber, CVD_Yt_O$_2$. In Figure 4, the obtained spectra of yttria coatings on W_f are compared with the reference spectra of yttrium oxide and tungsten oxide (mentioned as Ref. in Figure 4). The other intense peak around 967.40 cm^{-1} could also be assigned to yttrium oxide [33], but, so far, no concrete literature could be found to assign the peak at 1056.12 cm^{-1} to yttria, even though this peak is predominant in both CVD- and PVD-coated fibers.
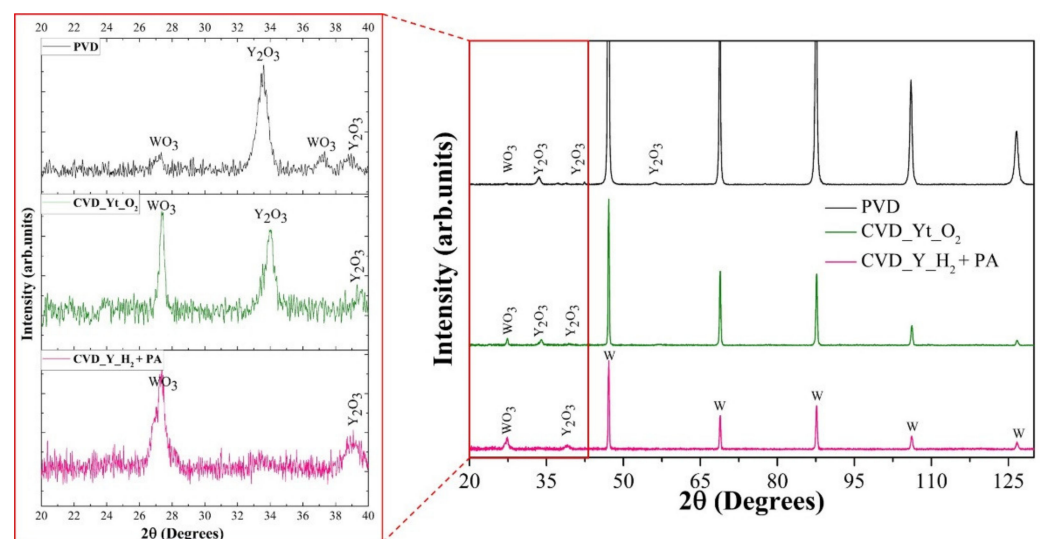

Figure 5. XRD diffractograms of CVD- and PVD-coated $WO_3/Y_2O_3/W_f$ (**right**); the 2θ region from 20° to 40° is plotted as a separate zoomed-in plot (**left**) to elucidate the diffraction peaks originating from the oxides.

3.3. XRD Phase Analysis

The X-ray diffraction patterns of CVD- and PVD-coated Y_2O_3/W_f are shown in Figure 5. As expected, in all the coated fibers, the cubic tungsten phase [34] of the W_f substrate is clearly detectable, as compared to the diffraction patterns of several 100 nanometer-thick WO_3/Y_2O_3 coatings detecting less intense peaks of cubic Y_2O_3 [35] and monoclinic WO_3 [36] phases. It has been observed that the diffraction peaks of cubic Y_2O_3 phase at 2θ angle 33.5° and 38.97° are evident in PVD and CVD_Yt_O$_2$ samples. Although the peak 33.5° is not prominently evident in CVD_Y_H$_2$ + PA samples, the diffraction peak at 2θ angle 38.97° is present, and it is related to the cubic phase of Y_2O_3. The monoclinic WO_3 diffraction peak at 2θ angle 27.3° is present in both PVD- and CVD-coated fibers, but the intensity of this peak varies (CVD_Y_H$_2$ + PA > CVD_Yt_O$_2$ > PVD), even though it is measured under exactly same experimental conditions. This observation is consistent with the microstructural analysis whereby the WO_3 is thinner in case of CVD_Yt_O$_2$ in comparison to the CVD_Y_H$_2$ + PA samples.

4. Conclusions

A comparative study on the fabrication and characterization of Y_2O_3 coatings on W_f through PVD and CVD routes is presented in this article. One advantage of the fabrication of Y_2O_3 coatings on W_f through PVD is that it operates at a lower temperature, and this helps to avoid the oxidation of W_f during the coating process. However, there are problems such as inhomogeneous coating along the axial length of the fiber surface and a slower coating rate that results in extensive material usage and a longer fabrication time. In such a case, CVD with possible advantages such as low production cost, less process complexity, minimal material usage, feasibility for upscaling, and reduced process times could be used as an alternative to PVD in the fabrication of Y_2O_3 on W_f. Nevertheless, a compensational formation of WO_3 as an interfacial layer between W_f and Y_2O_3 coatings, due to the high temperature used during the coating process, is still unavoidable. In this ongoing research to develop interfacial yttria coatings on W_f for the use in W_f/W composites, further investigations are already in progress. The research scope is set in upscaling the current discontinuous CVD to a continuous CVD, in which the latter is expected to offer more promising outcomes.

Institutional Review Board Statement: Not applicable.

Informed Consent Statement: Not applicable.

Data Availability Statement: The data that support the findings of this study are available from the corresponding author, upon reasonable request.

Conflicts of Interest: The authors declare no conflict of interest.

References

1. Andreani, R.; Diegele, E.; Laesser, R.; van der Schaaf, B. The European integrated materials and technology programme in fusion. *J. Nucl. Mater.* **2004**, *329*, 20–30. [CrossRef]
2. Coenen, J.W.; Antusch, S.; Aumann, M.; Biel, W.; Du, J.; Engels, J.; Heuer, S.; Houben, A.; Hoeschen, T.; Jasper, B.; et al. Materials for DEMO and reactor applications—boundary conditions and new concepts. *Phys. Scr.* **2016**, *2016*, 014002. [CrossRef]
3. Bolt, H.; Barabash, V.; Federici, G.; Linke, J.; Loarte, A.; Roth, J.; Sato, K. Plasma facing and high heat flux materials—Needs for ITER and beyond. *J. Nucl. Mater.* **2002**, *307*, 43–52. [CrossRef]
4. Bolt, H.; Barabash, V.; Federici, G.; Linke, J.; Loarte, A.; Roth, J.; Sato, K. Development of advanced high heat flux and plasma-facing materials. *Nucl. Fusion* **2017**, *57*, 092007.
5. Bolt, H.; Barabash, V.; Krauss, W.; Linke, J.; Neu, R.; Suzuki, S.; Yoshida, N.; ASDEX Upgrade Team. Materials for the plasma-facing components of fusion reactors. *J. Nucl. Mater.* **2004**, *329*, 66–73. [CrossRef]
6. Coenen, J.W.; Mao, Y.; Almanstötter, J.; Calvo, A.; Sistla, S.; Gietl, H.; Jasper, B.; Riesch, J.; Rieth, M.; Pintsuk, G.; et al. Advanced materials for a damage resilient divertor concept for DEMO: Powder-metallurgical tungsten-fiber reinforced tungsten. *Fusion Eng. Des.* **2017**, *124*, 964. [CrossRef]
7. Philipps, V. Tungsten as material for plasma-facing components in fusion devices. *J. Nucl. Mater.* **2011**, *415*, S2. [CrossRef]

8. Lässer, R.; Baluc, N.; Boutard, J.L.; Diegele, E.; Dudarev, S.; Gasparotto, M.; Möslang, A.; Pippan, R.; Riccardi, B.; Van Der Schaaf, B. Structural materials for DEMO: The EU development, strategy, testing and modelling. *Fusion Eng. Des.* **2007**, *82*, 511. [CrossRef]

9. Maisonnier, D.; Cook, I.; Pierre, S.; Lorenzo, B.; Edgar, B.; Karin, B.; Robin, F.; Luciano, G.; Stephan, H.; Claudio, N.; et al. The European power plant conceptual study. *Fusion Eng. Des.* **2005**, *75*, 1173–1179. [CrossRef]

10. Du, J. A Feasibility Study of Tungsten-Fiber-Reinforced Tungsten Composites with Engineered interfaces. *Dissertation* **2010**.

11. Riesch, J.; Buffiere, J.Y.; Höschen, T.; Di Michiel, M.; Scheel, M.; Linsmeier, C.; You, J.H. In situ synchrotron tomography estimation of toughening effect by semi-ductile fiber reinforcement in a tungsten-fiber-reinforced tungsten composite system. *Acta Mater.* **2013**, *61*, 7060. [CrossRef]

12. Mao, Y.; Coenen, J.W.; Riesch, J.; Sistla, S.; Almanstötter, J.; Jasper, B.; Terra, A.; Höschen, T.; Gietl, H.; Linsmeier, C.; et al. Influence of the interface strength on the mechanical properties of discontinuous tungsten fiber-reinforced tungsten composites produced by field assisted sintering technology. *Compos. Part A Appl. Sci. Manuf. S* **2018**, *107*, 342. [CrossRef]

13. Stang, H.; Shah, S.P. Failure of fiber-reinforced composites by pull-out fracture. *J. Mater. Sci.* **1986**, *21*, 953. [CrossRef]

14. Chawla, K.K. *Composite Materials*; Springer: Berlin/Heidelberg, Germany, 2019; p. 251.

15. Li, V.C.; Wang, Y.; Backer, S. A micromechanical model of tension-softening and bridging toughening of short random fiber reinforced brittle matrix composites. *J. Mech. Phys. Solids* **1991**, *39*, 607. [CrossRef]

16. Shimoda, K.; Park, J.S.; Hinoki, T.; Kohyama, A. Influence of pyrolytic carbon interface thickness on microstructure and mechanical properties of SiC / SiC composites by NITE process. *Compos. Sci. Technol.* **2008**, *68*, 98. [CrossRef]

17. Czél, G.; Wisnom, M.R. Demonstration of pseudo-ductility in high performance glass/epoxy composites by hybridization with thin-ply carbon prepreg. *Compos. Part A Appl. Sci. Manuf. S* **2013**, *52*, 23. [CrossRef]

18. Du, J.; Höschen, T.; Rasinski, M.; Wurster, S.; Grosinger, W.; You, J.H. Feasibility study of a tungsten wire-reinforced tungsten matrix composite with ZrO_x interfacial coatings. *Compos. Sci. Technol.* **2010**, *70*, 1482. [CrossRef]

19. Zhu, J.; Zhu, Y.; Shen, W.; Wang, Y.; Han, J.; Tian, G.; Lei, P.; Dai, B. Growth and characterization of yttrium oxide films by reactive magnetron sputtering. *Thin Solid Film.* **2011**, *519*, 4894. [CrossRef]

20. Wang, L.; Pan, Y.; Ding, Y.; Yang, W.; Mao, W.L.; Sinogeikin, S.V.; Meng, Y.; Shen, G.; Mao, H.K. High-pressure induced phase transitions of Y_2O_3 and Y_2O_3:Eu^{3+}. *Appl. Phys. Lett.* **2009**, *94*, 061921. [CrossRef]

21. Barve, S.A.; Mithal, N.; Deo, M.N.; Biswas, A.; Mishra, R.; Kishore, R.; Bhanage, B.M.; Gantayet, L.M.; Patil, D.S. Effects of precursor evaporation temperature on the properties of the yttrium oxide thin films deposited by microwave electron cyclotron resonance plasma assisted metal—organic chemical vapor deposition. *Thin Solid Film.* **2011**, *519*, 3011. [CrossRef]

22. Yan, F.; Liu, Z.T.; Liu, W.T. Structural and optical properties of yttrium trioxide thin films prepared by RF magnetron sputtering. *Vacuum* **2011**, *86*, 72. [CrossRef]

23. Bose, P.P.; Gupta, M.K.; Mittal, R.; Rols, S.; Achary, S.N.; Tyagi, A.K.; Chaplot, S.L. Phase transitions and thermodynamic properties of yttria, Y2O3: Inelastic neutron scattering shell model and first-principles calculations. *Phys. Rev. B* **2011**, *84*, 094301. [CrossRef]

24. Forrest, R.A.; Tabasso, A.; Danani, C.; Jakhar, S.; Shaw, A.K. Handbook of activation data calculated using EASY-2007. *UKAEA FUS* **2009**, *552*, 399.

25. Abdulagatov, A.I.; Amashaev, R.R.; Ashurbekova, K.N.; Ramazanov, S.M.; Palchaev, D.K.; Maksumova, A.M.; Rabadanov, M.K. Atomic Layer Deposition of Y_2O_3 Using Tris(butylcyclopentadienyl)yttrium and Water. *Russ. Microelectron.* **2019**, *48*, 1–2. [CrossRef]

26. Lei, P.; Leroy, W.; Dai, B.; Zhu, J.; Chen, X.; Han, J.; Depla, D. Study on reactive sputtering of yttrium oxide: Process and thin film properties. *Surf. Coat. Technol.* **2015**, *276*, 39–46. [CrossRef]

27. Fernandez, Y.D.; Sun, L.; Gschneidtner, T.; Moth-Poulsen, K. Research update: Progress in synthesis of nanoparticle dimers by self-assembly. *APL Mater.* **2014**, *2*, 1. [CrossRef]

28. Mao, Y.; Engels, J.; Houben, A.; Rasinski, M.; Steffens, J.; Terra, A.; Linsmeier, C.; Coenen, J.W. The influence of annealing on yttrium oxide thin film deposited by reactive magnetron sputtering: Process and microstructure. *Nucl. Mater. Energy* **2017**, *10*, 1. [CrossRef]

29. Berg, S.; Nyberg, T. Fundamental understanding and modeling of reactive sputtering processes. *Thin Solid Film.* **2005**, *476*, 215. [CrossRef]

30. Safi, I. Recent aspects concerning DC reactive magnetron sputtering of thin films: A review. *Surf. Coat. Technol.* **2000**, *127*, 203. [CrossRef]

31. Rasband, W.S. *ImageJ*; U.S. National Institutes of Health: Bethesda, MD, USA, 1997–2018. Available online: https://imagej.nih.gov/ij/ (accessed on 15 July 2021).

32. Mariscal-Becerra, L.; Acosta-Najarro, D.; Falcony-Guajardo, C.; Sanchez, H.M. Luminescent and structural analysis of yttrium oxide doped with different percentages of terbium and dysprosium, to obtain different shades of green to yellow. *J. Nanophotonics* **2018**, *12*, 1. [CrossRef]

33. Xu, J.Q.; Xiong, S.J.; Wu, X.L.; Li, T.H.; Shen, J.C.; Chu, P.K. Investigation of activated oxygen molecules on the surface of Y_2O_3 nanocrystals by Raman scattering. *J. Appl. Phys.* **2013**, *114*, 093512. [CrossRef]

34. Tatge, S. XRD Database [PDF00-004-0806]. *Natl. Bur. Stand. U.S. Circ.* **1953**, *539*, 28.

35. Martin, K.; McCarthy, G. *XRD Database [PDF00-041-1105]; ICDD Grant-in-Aid*; North Dakota State University: Fargo, ND, USA.

36. Booth, J. XRD Database [PDF00-036-0103]. *J. Solid State Chem.* **1982**, *41*, 293.